IEEE Access
Multidisciplinary ⁝ Rapid Review ⁝ Open Access Journal

Received June 28, 2019, accepted July 29, 2019, date of publication August 9, 2019, date of current version August 26, 2019.

Digital Object Identifier 10.1109/ACCESS.2019.2934185

Comparison of Current Control Strategies Based on FCS-MPC and D-PI-PWM Control for Actively Damped VSCs With LCL-Filters

CHEE SHEN LIM[1], (Member, IEEE), SZE SING LEE[2], (Senior Member, IEEE),
YI CHYN CASSANDRA WONG[1], (Student Member, IEEE),
INAM ULLAH NUTKANI[3], (Senior Member, IEEE),
AND HUI HWANG GOH[4], (Senior Member, IEEE)
[1]University of Southampton Malaysia, Iskandar Puteri 79200, Malaysia
[2]Newcastle Research & Innovation Institute, Newcastle University in Singapore, Singapore 609607
[3]School of Engineering, Royal Melbourne Institute of Technology, Melbourne, VIC 3000, Australia
[4]School of Electrical Engineering, Guangxi University, Nanning 530015, China

Corresponding authors: Chee Shen Lim (c.s.lim@soton.ac.uk) and Hui Hwang Goh (hhgoh@gxu.edu.cn)

This work was supported in part by the Ministry of Education Malaysia (through the Fundamental Research Grant Scheme) and in part by the School of Electrical Engineering, Guangxi University, China.

ABSTRACT This paper presents a comparative study of the proportional-integral-based (PI-based) synchronous current control strategy with derivative-feedback-based active damping and the finite-control-set model-predictive-control-based (FCS-MPC-based) synchronous current control strategy with cost-function-based active damping. For a fair comparison, the sensor requirement and the average switching frequency of FCS-MPC are made equivalent to that of the pulse-width-modulation-based counterpart through internal model estimation and control sampling frequency adjustment. The comparative study considers gain/weighting-factor tuning, delay compensation, switching harmonics, and active damping performance at the critical frequency operating point. The overall performance of both schemes is validated through the same experimental setup and test scenarios. The results conclude that the emerging FCS-MPC has the potential to produce similar results as the classical PI-based counterpart while carrying some practical features. These include being intuitive in active damping design and tuning, guaranteeing fast dynamics, and being sufficiently robust to grid impedance shifting. These findings essentially justify the potential of model predictive control being a viable alternative for this area of application.

INDEX TERMS Model predictive control, cost function, LCL filter, active damping, derivative voltage feedback.

I. INTRODUCTION

Grid-connected voltage source converter (VSC) is the main mechanism to interface distributed generation with the power grid. It is well established that the power density and efficiency improvement of the power converter system can be improved by removing the physical damper resistance. However, it is known that the actual implementation of the damper-free system (e.g. a VSC with an LCL filter) would, due to inherent computational and PWM delays and with improperly tuned gain parameters, suffer from filter resonance or control instability [1].

Two current strategies are possible: converter current control and grid current control. Converter current control will be the focus here as it carries the advantage of only requiring one set of current sensors to realize both current control and over-current protection [2]. Depending on which current control strategy, slightly different active damping control design applies. In general, control-based active damping techniques can be categorized, according to [1], as single-loop and multi-loop techniques. In essence, the former is about improving the gain/phase margin of the delayed system through the introduction of filters being inserted in series with the forward-path controllers (i.e. main current controllers). It includes e.g. notch filter [3]–[5] and lead-lag compensator [7]. The latter appears mostly in the form of

---

The associate editor coordinating the review of this article and approving it for publication was Alfeu J. Sguarezi Filho.

feedback-path controllers/filters with multi-loop [7]–[16] or single-loop [17]–[21] feedback structure. Examples include the capacitor-voltage-based discrete derivative feedback and its variants [7]–[9], capacitor-current-based proportional feedback and its variants [10]–[15], lead-lag network [2] and biquad filter [16], virtual impedance damping and its variants [17]–[21], passivity-based approach [16], internal model based approach [22], and combination of notch filter and derivative feedback [5]. Moreover, hybrid passive-active damping, which is particularly relevant for weak grid applications, are also available [23], [24]. The analysis tools involved are essentially the frequency-domain methods, such as root locus, bode diagram and Nyquist plot. About the main current controllers, proportional-integral [3], [7], [16] and proportional-resonant [12], [13], [17] controllers are common. Note also that there are active damping controls for higher-order filters [22], [23] but the focus of this work will be on the standard LCL solution.

In recent years, the emerging model predictive control (MPC) has been studied actively in conjunction with grid-connected converters with LCL filters (with and without active damping consideration) [25]–[31]. Its uniqueness include the time-domain approach, predictive nature, and cost-function-based control feature. Two basic variants of MPC with active-damping consideration have been reported to date: finite-control-set (FCS) MPC [25]–[29] and continuous-control-set (CCS) MPC [30]. Authors in [25]–[28] have investigated the possibilities of appending the virtual resistance based active damping techniques to FCS-MPC. Specifically, [26] focuses on low-frequency long-horizon finite-control-set MPC meant for medium-voltage grids. FCS-MPC schemes with two prediction horizons that simultaneously control three-vector-variables (i.e. complex variables) consisting the converter current vector, grid current vector, and capacitor voltage vectors, are proposed in [27], [29]. On the other hand, [28] showed that a two-vector-variables cost function can readily provide active damping without virtual-resistance method, and that the converter switching frequency can be directly manipulated through a weighted cost function. The results in [30] have also supported the finding on cost-function-based active damping – a two-vector cost function that considers both the inverter current and voltage input can provide the necessary active damping effect.

Despite the above establishment, the relative control and active damping performance between the MPC schemes with unique cost-function-based active damping capability (e.g. the two-vector cost function in [28], [30] and the three-vector cost function in [27], [29]) and the existing frequency-domain-based state of the arts [6]–[16] have never been comprehensively compared. This paper intends to contribute to this aspect by designing and assessing the two inverter current control strategies from these categories on a common hardware setting, i.e. the same filter parameters, microprocessor, converter setup, and operating points. The assessment will include their design principle, active damping level, tracking performance, and robustness. In the FCS-MPC-based control strategy, the inverter current control and active damping will be commonly realized through the cost function; in the second control strategy, the inverter current control is realized through PI controllers while the active damping is achieved through derivative-capacitor-voltage-based mechanism (known as D-PI-PWM control in this paper) [8]–[10]. From the existing FCS-MPC schemes [27]–[29], [31], it is established that the typical control schemes, owing to full state requirement, would require more sensors than the classical state-of-the-art techniques. This work exploits the internal predictive model to achieve sensor-count reduction, ensuring a fair comparison. On the other hand, for D-PI-PWM control, frequency-domain design analysis and symmetrical optimum tuning will be used for the control design. A simple yet effective discrete derivative controller based on hardware oversampling capability has been designed here to approximate the continuous-time derivative controller. Apart from the design methodology, the steady-state and transient performance, active damping performance, and the effect of grid-impedance shifting will be analyzed and compared.

The rest of the paper is organized as follows: Section II describes the design of FCS-MPC with cost-function-based active damping. Section III describes the design of the PI control scheme with derivative-capacitor-voltage-feedback-based active damping. Section IV shows and analyzes selected simulation results of both control schemes. Section V presents the experimental results and summarizes the comparison. Section VI concludes the paper.

II. FCS-MPC STRATEGY

A. PREDICTIVE MODEL AND COST FUNCTION

A grid-connected two-level VSC with an LCL filter is shown in Fig. 1. The system is modelled in the synchronous reference frame as the theoretical MPC is typically derived based on DC variables regulation/tracking. To start with, the continuous-time state-space model of the system is given by:

$$\dot{\mathbf{x}}(t) = \mathbf{A}\mathbf{x}(t) + \mathbf{B}_1\mathbf{u}(t) + \mathbf{B}_2\mathbf{v}(t) \tag{1}$$

with

$$\mathbf{A} = \begin{bmatrix} -\frac{R_1}{L_1} & 2\pi f_g^* & 0 & 0 & -\frac{1}{L_1} & 0 \\ -2\pi f_g^* & -\frac{R_1}{L_1} & 0 & 0 & 0 & -\frac{1}{L_1} \\ 0 & 0 & -\frac{R_2}{L_2} & 2\pi f_g^* & \frac{1}{L_2} & 0 \\ 0 & 0 & -2\pi f_g^* & -\frac{R_2}{L_2} & 0 & \frac{1}{L_2} \\ \frac{1}{C} & 0 & -\frac{1}{C} & 0 & 0 & 2\pi f_g^* \\ 0 & \frac{1}{C} & 0 & -\frac{1}{C} & -2\pi f_g^* & 0 \end{bmatrix}$$

$$\mathbf{B}_1 = \begin{bmatrix} 1/L_1 & 0 & 0 & 0 & 0 & 0 \\ 0 & 1/L_1 & 0 & 0 & 0 & 0 \end{bmatrix}^T$$

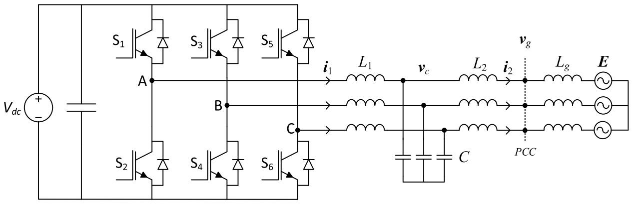

FIGURE 1. A voltage source inverter with an LCL filter and a constant DC source.

TABLE 1. System and control parameters.

Symbols	Parameters	Values
V_{dc}	DC supply voltage	350 V
-	Grid phase/line-to-line voltage	120 V/208V
V_{base}, I_{base}	Base voltage, base current	202.1 V, 10 A
F_s	Control sampling frequency	2.5kHz, 20 kHz
L_1 (R_1)	Converter-side inductance (internal resistance)	7.35 mH (0.291 Ω)
L_2 (R_2)	Grid-side inductance (internal resistance)	2.94 mH (0.0649 Ω)
C	Filter capacitance	30 µF
F_{res}	L_1CL_2 resonant frequency	634 Hz
-	L_2C resonant frequency	536 Hz
$F_{crit\ PWM}$	D-PI-PWM's critical frequency	416.7 Hz
$u_{d\min}/u_{d\max}$	PI's *d*-axis upper/lower limits (pu)	±184 V or 0.91pu
$u_{q\min}/u_{q\max}$	PI's *q*-axis upper/lower limits (pu)	±83 V or 0.41pu
-	Digital differentiator's computational frequency	25 kHz

$$\mathbf{B}_2 = \begin{bmatrix} 0 & 0 & -1/L_2 & 0 & 0 & 0 \\ 0 & 0 & 0 & -1/L_2 & 0 & 0 \end{bmatrix}^T$$

where $\mathbf{x}$ is the state vector consisting the converter current variable $\boldsymbol{i}_1$, grid current variable $\boldsymbol{i}_2$, and filter capacitor voltage variable $\boldsymbol{v}_c$, i.e. $\mathbf{x} = [i_{1d}\ i_{1q}\ i_{2d}\ i_{2q}\ v_{cd}\ v_{cq}]^{\mathrm{T}}$; $\mathbf{y}$ is the output vector containing $\boldsymbol{i}_1$ and $\boldsymbol{v}_{\mathbf{c}}$, i.e. $\mathbf{y} = [i_{1d}\ i_{1q}\ v_{cd}\ v_{cq}]^{\mathrm{T}}$; $\mathbf{u}$ is the control input set consisting the converter output voltage $\boldsymbol{u}_{\mathbf{c}}$, i.e. $\mathbf{u} = [u_{cd} u_{cq}]^{\mathrm{T}}$; $\mathbf{v}$ is the disturbance vector consisting of the grid voltage variable $\boldsymbol{v}_{\mathbf{g}}$, i.e. $\mathbf{v} = [v_{gd} v_{gq}]^{\mathrm{T}}$. $\mathbf{A}$, $\mathbf{B}_1$, and $\mathbf{B}_2$, are the time-invariant (practically) state-, input-, and disturbance-coefficients. Note that the grid-side and converter-side parasitic resistances R_1 and R_2, which are usually very small in value, are nevertheless included here for generality. f_g^* is the rated grid frequency. Parameters of the whole system considered in this work are listed in Table 1. Subsequently, full-order discretization technique is applied here to obtain the discrete state-space model:

$$\mathbf{x}_{k+1} = \mathbf{F}\mathbf{x}_k + \mathbf{G}_1\mathbf{u}_k + \mathbf{G}_2\mathbf{v}_k \tag{2}$$

where

$$\begin{aligned} \mathbf{F} &= e^{\mathbf{A}T} \\ \mathbf{G}_1 &= \mathbf{A}^{-1}(\mathbf{F} - \mathbf{I})\mathbf{B}_1 \\ \mathbf{G}_2 &= \mathbf{A}^{-1}(\mathbf{F} - \mathbf{I})\mathbf{B}_2 \end{aligned}$$

Since $\mathbf{A}$, $\mathbf{B}_1$, and $\mathbf{B}_2$ are time-variant, $\mathbf{F}$, $\mathbf{G}_1$, and $\mathbf{G}_2$ can be readily computed using numerous software packages (*Matlab* is used in this case).

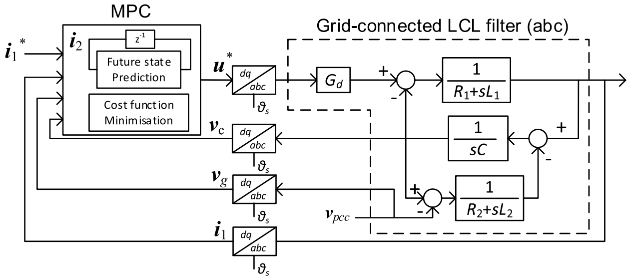

FIGURE 2. Finite-control-set model predictive converter current control with cost-function-based active damping.

In the beginning of every sampling instant, the measured phase variables will be first transformed through the decoupling transformation (3) to produce the stationary-axis variables (with zero-sequence component omitted), followed by the rotational transformation (4) to produce the synchronous-axis variables:

$$\boldsymbol{f}_{\alpha\beta,k} = \begin{bmatrix} f_{\alpha,k} \\ f_{\beta,k} \end{bmatrix} = \frac{2}{3} \begin{bmatrix} 1 & -\frac{1}{2} & -\frac{1}{2} \\ 0 & \frac{\sqrt{3}}{2} & -\frac{\sqrt{3}}{2} \end{bmatrix} \begin{bmatrix} f_{a,k} \\ f_{b,k} \\ f_{c,k} \end{bmatrix} \tag{3}$$

$$\boldsymbol{f}_k = \begin{bmatrix} f_{d,k} \\ f_{q,k} \end{bmatrix} = \begin{bmatrix} \cos\theta_{s,k} & \sin\theta_{s,k} \\ -\sin\theta_{s,k} & \cos\theta_{s,k} \end{bmatrix} \begin{bmatrix} f_{\alpha,k} \\ f_{\beta,k} \end{bmatrix} \tag{4}$$

where θ_s is the instantaneous grid voltage's angular position provided by the phase-locked loop (PLL); f_a, f_b, and f_c are the generic phase variables (only two phases are measured while the third phase is calculated by exploiting the isolated neutral property); f_α and f_β are the stationary-axis variables; k subscript indicates the sampling instant. $\boldsymbol{f}_{\alpha\beta}$ and $\boldsymbol{f}$ are the generic stationary-axis and synchronous-axis space-vector variables. The converter phase voltages can be obtained from the switching state as below:

$$u_i = \frac{V_{dc}}{3} \begin{bmatrix} 2 & -1 & -1 \\ -1 & 2 & -1 \\ -1 & -1 & 2 \end{bmatrix} \begin{bmatrix} s_a \\ s_b \\ s_c \end{bmatrix} \tag{5}$$

where $s_i = [0, 1]$, $i = a, b$, or c.

Expression (2) is used to predict the state variables at the first prediction horizon using the state variable feedbacks and the grid voltage feedbacks, and the prediction can be repeated for the second horizon and onwards. However, to avoid exponential growth of the real-time computational complexity, both the control and prediction horizons are limited to only one. Unlike the control horizon, the prediction horizon can be made longer than one without incurring an exponential (only linear) increase in computational burden, but it was found out in the simulation study that increasing the prediction horizon does not lead to an appreciable improvement in the converter current tracking or the active damping performance. In addition, it is worth highlighting that if grid current control is desired, a minimum of two (or three, depending on what discretization technique is used) prediction horizons is necessary. Fig. 2 shows the schematic for the FCS-MPC scheme considered here.

The cost function that considers all the predicted variables is shown below [27]–[29]:

$$\begin{aligned}\min_{\mathbf{u}} J = {} & w_1(i^*_{1d,k+1} - i_{1d,k+1})^2 + w_1(i^*_{1q,k+1} - i_{1q,k+1})^2 \\ & + w_2(v^*_{cd,k+1} - v_{cd,k+1})^2 + w_2(v^*_{cq,k+1} - v_{cq,k+1})^2 \\ & + w_3(i^*_{2d,k+1} - i_{2d,k+1})^2 + w_3(i^*_{2q,k+1} - i_{2q,k+1})^2\end{aligned} \tag{6}$$

The choice of weighting factors in this work is illustrated below. The LCL network with unconnected capacitor neutral has two degrees of freedom, i.e. only two variables can be independently controlled if voltages at the two ends of the filter network are fully controllable. However, since the grid voltage is not controllable, only one degree of freedom remains. The control problem hence reduces to a SISO form. In principle, the cost function should then be reduced to consist only the converter current error while maintaining the ability to ensure error-free tracking (average). However, the resulted performance will not be satisfactory due to filter resonance, as confirmed by the simulation and experimental results (in next sections).

For an LCL-VSC system with closed-loop converter current control structure, two resonant frequencies are relevant:

$$f_{L_1CL_2'} = \frac{1}{2\pi}\sqrt{\frac{L_1 + L_2'}{L_1CL_2'}} \quad \text{and}\, f_{L_2'C} = \frac{1}{2\pi}\frac{1}{\sqrt{L_2'C}} \tag{7}$$

where L_2' is the total grid-side inductance. To achieve cost-function-based active damping, the controller must be able to account for the presence of the resonant harmonics of either the capacitor voltage or the grid current within the prediction horizons. If either of them is regulated, then the resonance will be suppressed. In this work, the capacitor voltage error is chosen because the sensor requirement is the same as that in the classical D-PI-PWM control:

$$\begin{aligned}\min_{\mathbf{u}} J = {} & (i^*_{1d,k+1} - i_{1d,k+1})^2 + (i^*_{1q,k+1} - i_{1q,k+1})^2 \\ & + w_2(v^*_{cd,k+1} - v_{cd,k+1})^2 + w_2(v^*_{cq,k+1} - v_{cq,k+1})^2\end{aligned} \tag{8}$$

It can be noticed that once w_1 is set to one then w_2 is the only weighting factor left for tuning. Note also that (8) is similar to one of the state-variable combinations considered in [28] but is different from those in [27], [29] in which three-vector variables are considered. In the simulation study (Section IV), it will be shown that w_2 can be set to a very high value, e.g. up to and beyond 100, and the closed-loop control continues to work well. However, this behavior cannot be replicated in the experiment. It is found that the range of usable w_2 weighting factor is significantly reduced and the cause of such discrepancy is deduced to be the existence measurement errors and noises. This observation hints that analytical tuning of weighing factor tuning (which is one of the recent research trends for various power electronic applications) will only be relevant if the non-ideal phenomenon is accurately modelled in the predictive model. This is however beyond the intended scope of this paper but is indeed one recommended future work. Next, the setting of the variable references, which is relevant to ensure current control and active damping, is considered.

The standard operational practice of compensating the filter's reactive power applies here and this requires the setting of the future converter current references (that are assumed constant throughout the prediction horizon) in the following manner:

$$\boldsymbol{i}^*_{1,k+1} = \boldsymbol{i}^*_{1,k} = \boldsymbol{i}^*_{2,k} + j\omega_s C \cdot \hat{\boldsymbol{v}}_{c,k} \tag{9}$$

where $\omega_s = 2\pi f^*_g$. Eq. (9) is essentially meant to realize an indirect grid current control. One known drawback (as compared to the direct grid current control method) is that the capacitance value of the filter capacitor and the grid's synchronous frequency value are required for the reference calculation. The synchronous frequency value can be obtained accurately through the PLL. The filter capacitance, on the other hand, usually only deviates rather insignificantly throughout the operation.

In order to avoid the resonance harmonics in transient to appear directly in the converter current reference, the capacitor voltage should first be low-pass-filtered:

$$\hat{\boldsymbol{v}}_{c,k} = \left(\frac{F_s}{F_s + F_c}\right)\hat{\boldsymbol{v}}_{c,k-1} + \left(\frac{F_c}{F_s + F_c}\right)\boldsymbol{v}_{c,k} \tag{10}$$

F_s is the control sampling frequency and F_c is the digital low-pass filter's cut-off frequency which should be chosen lower than the resonant frequency. Grid current reference $\boldsymbol{i}^*_{2,k}$ is supplied from the outer active and reactive power control loop (not used here though).

Next, the steady-state capacitor voltage reference can be obtained by applying Kirchoff's voltage law at the L_2C network:

$$\boldsymbol{v}^*_{c,k+1} = \boldsymbol{v}^*_{c,k} = R_2\boldsymbol{i}^*_{2,k} + j\omega_s L_2\boldsymbol{i}^*_{2,k} + \boldsymbol{v}_{g,k} \tag{11}$$

where the grid voltage needs to be assumed constant throughout the prediction horizon. With the above reference setting, FCS-MPC's cost function is expected to achieve the converter current tracking while being able to suppress the filter resonance.

B. SENSOR COUNT REDUCTION

The existing FCS-MPC schemes with cost-function-based active damping [27]–[29] typically use four sets of sensors (a minimum of two sets of voltage sensors and two sets of current sensors, with the sensor count being eight) while the frequency-domain techniques with capacitor-voltage-feedback-based active damping use primarily three sets of sensors (a minimum of two sets of voltage sensors and one set of current sensors, with the sensor count being six) [7]–[9]. In this work, it will be shown that the grid current feedback in (2) can be readily provided by the internally estimated grid current variable, serving as an unmeasurable feedback, as already depicted in Fig. 2. At k^{th} sampling instant, the grid current state variable $\boldsymbol{i}_{2,k|k}$ (i.e. $i_{2d,k}$ and $i_{2q,k}$) will be obtained from the previously estimated values, $\boldsymbol{i}_{2,k|k-1}$. It has been verified in the simulation that the FCS-MPC scheme produces identical results (in ideal, simulation environment) as compared to the one with sensor measurement; hence, all the subsequent simulation and experimental studies have been obtained with the proposed reduced-sensor-count simplification. This ensures a fair comparison in terms of hardware requirement.

C. COMPUTATIONAL AND PWM DELAY COMPENSATION

MPC implementation in power electronic applications, owing to non-negligible computational time, is often accompanied by one-step digital implementation delay [27]–[30]. The standard way of delay compensation is through the one-step-ahead estimation where, in the start of every k^{th} control cycle, the state variables at k^{th} sampling instant $\mathbf{x}_k$, together with the previously chosen optimal voltage vector $\boldsymbol{u}_k$ (to be precise, being $\boldsymbol{u}_{k|k-1}$), will be used to estimate the state variables at $(k+1)^{th}$ prediction horizon $\mathbf{x}_{k+1}$. Then, the full MPC algorithm is initiated at the $(k+1)^{th}$ prediction horizon where complete enumeration of the finite control inputs $\mathbf{u}_{k+1}$ takes place. Cost function (8) will evaluate the cost errors based on the predicted state variable $\mathbf{x}_{k+2}$. These steps are summarized as follows:

$$\begin{aligned} &\textit{First step}: & \mathbf{x}_{k+1} &= \mathbf{F}\mathbf{x}_k + \mathbf{G}_1\mathbf{u}_k + \mathbf{G}_2\mathbf{v}_k \\ &\textit{Second step}: & \mathbf{x}_{k+2} &= \mathbf{F}\mathbf{x}_{k+1} + \mathbf{G}_1\mathbf{u}_{k+1} + \mathbf{G}_2\mathbf{v}_{k+1} \end{aligned} \tag{12}$$

where

$$\mathbf{v}_{k+1} = \mathbf{v}_k, \quad \mathbf{u}_k = [\boldsymbol{u}_k] = \left[\boldsymbol{u}_{\alpha\beta,k} \cdot \boldsymbol{e}^{-j\theta_s}\right],$$

and

$$\mathbf{u}_{k+1} = [\boldsymbol{u}_{k+1}] = \left[\boldsymbol{u}_{\alpha\beta,k+1} \cdot \boldsymbol{e}^{-j(\theta_s+\omega_s T)}\right]$$

Note that all actual voltage vectors shall be rotationally transformed at $(\theta_s+\omega_s T)$ rad to account for the inherent single sampling delay where ω_s is the angular frequency of the grid voltage vector. At the end of the optimization cycle, the switching state or the converter voltage vector that produces the lowest cost in (8) will be selected and be actuated in the beginning of $(k+1)^{th}$ control cycle. With receding horizon mechanism, the whole process will then be repeated at the next control cycle.

III. D-PI-PWM CONTROL STRATEGY

A. OVERALL CONTROL SCHEMATIC

This work uses synchronous PI control with derivative-capacitor-voltage feedback as the candidate for the comparative study. Fig. 3a shows the overall D-PI-PWM control block diagram. What follows briefly explains the tuning steps required for the three gain parameters, K_p, τ_i, and K_{ad}. The converter voltage reference $\boldsymbol{u}^*_{\alpha\beta}$ is obtained as follows:

$$\begin{aligned} \boldsymbol{u}^*_{PI} &= F(s)\cdot(\boldsymbol{i}^*_1 - \boldsymbol{i}_1) + j\omega_s L_1 \boldsymbol{i}_1 \\ \boldsymbol{u}^*_{\alpha\beta} &= \boldsymbol{u}^*_{PI} e^{j\theta_s} + H(s)\cdot \boldsymbol{v}_{c,\alpha\beta} \end{aligned} \tag{13}$$

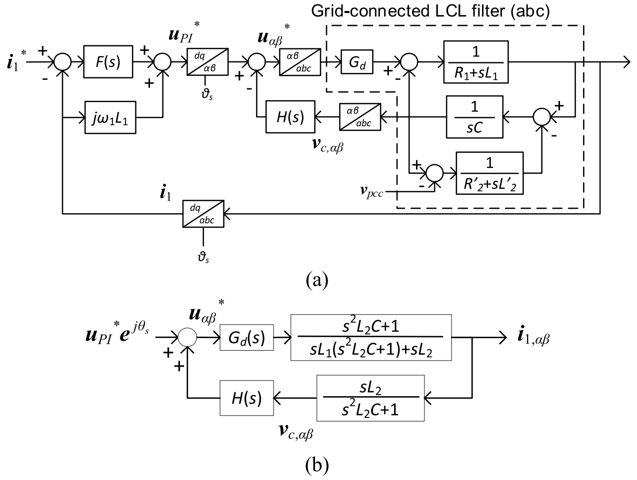

FIGURE 3. **(a) PI-based converter current control scheme with derivative-feedback active damping. ($R'_2 + sL'_2$) is the sum of the filter's grid-side impedance and the equivalent grid impedance; (b) Inner loop for active damping analysis.**

with

$$\begin{aligned} F(s) &= K_p\left(1+\frac{1}{\tau_i s}\right) \\ H(s) &= sCK_{ad} \end{aligned}$$

where θ_s is the synchronous reference frame's angular position obtained from PLL (as already explained in Section II-A). The tuning steps can be summarized into two stages: first, K_{ad} value is selected based on pole placement through root locus analysis; second, K_p and τ_i are selected by applying the symmetrical optimum tuning method.

B. TUNING OF ACTIVE DAMPING AND MAIN CURRENT CONTROLLERS

The effect of K_{ad} gain on active damping can be analyzed by applying the root locus analysis on the open-loop transfer function of the active-damping control loop. The worst-case scenario is assumed in which all filter parasitic resistances are assumed zero/negligible. Based on Fig. 3b, the open-loop transfer function is:

$$T_{OL} = \frac{K_{ad} G_d s}{L_1\left(s^2+\omega_{res}^2\right)} \tag{14}$$

where

$$\omega_{res} = \sqrt{\frac{L_1+L_2}{L_2 L_1 C}} \quad \text{and } G_d = e^{-T_d s} \approx \frac{1-T_d s/2 + T_d^2 s^2/36}{1+T_d s/2+T_d^2 s^2/36}$$

For further analysis, delay G_d can be approximated by the second-order Padé approximants and T_d is essentially $1.5T_s$ [1]. Eq. (14) is discretized (e.g. through zero-order-hold in numerical software package) and the discrete-time root loci in Fig. 4 is obtainable. Fig. 4a shows the case with the equivalent grid reactance assumed zero. This means only the filter's grid-side impedance exists at the output stage. As expected, it is shown clearly that after the maximum allowable K_{ad} the

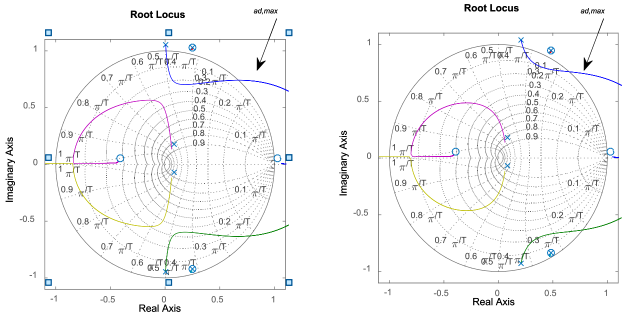

FIGURE 4. Effect of shifting effective grid impedance, $L_2' = L_2 + L_g$, on the active damping loop: (left) $L_g = 0$ mH, (right) $L_g = 0.5L_2'$.

closed-loop system will become unstable. Fig. 4b is meant to illustrate the effect of non-zero grid reactance or varying grid impedance cases on K_{ad} margin (a.k.a. $K_{ad,max}$ here). The equivalent grid reactance is assumed to be 50% of the filter grid-side impedance and it can be noticed that $K_{ad,max}$ has reduced significantly (from 53 to 35). Therefore, the recommended K_{ad} range is about 5 to 10, with the upper limit meant for providing margin for L_g variation. With this range (and with $L_g = 0$), the dominant poles should have a damping coefficient within the range of 0.1 to 0.29.

It is well known that sampling-based implementation of the derivative term requires additional design consideration on ensuring stability while keeping the phase margin and stability. Numerous works have been developed in the past: backward-Euler discrete derivative [7], lead/lag compensator [2], biquad digital filter [16], quadrature-second-order generalized integrator [8], indirect non-ideal generalized integrator [32], and other hybrid methods [9]. However, this work adopts a significantly simpler but equally accurate approach – one that exploits the hardware oversampling capability into closely approximating the derivative term. The differentiator is oversampled and implemented with backward-Euler discretization at ten times the main control sampling frequency F_s. Low-pass filter(s) are then appended to improve the stability at high frequency (i.e. to keep the overall gain below 0 dB at the phase crossover frequency).

$$H_1(s) = sCK_{ad}\left(\frac{\omega_c}{s+\omega_c}\right)^m \tag{15}$$

m is the number of first-order low-pass filters, and a maximum of 2 is considered here. The recommended cut-off frequencies f_c should be significantly higher than the nominal resonant frequency (i.e. with $L_g = 0$). In this work, a value of 6.25 kHz (i.e. about $10F_{res}$) is recommended here. Bode diagram of $H_1(s)$ for $m = 1$ and 2, together with $H(s)$ from (12) and another well-established lead compensator controller $H_2(s)$ (obtained from [15]), are summarized in Fig. 5. H_2 takes the form of $K_{ad}C\omega_{res}(s + k_f\omega_{res})/(k_f s + \omega_{res})$ with $k_f = \sqrt{[(1 - \sin\varphi_{res})/(1 + sin\varphi_{res})]}$. It can be seen that, below the resonant frequency of 634 Hz, gain and phase characteristics for both H_1 closely resembles that of H, closer than that of H_2. The close resemblance also means that the proposed H_1 can deal with the shifting of L_g (i.e. lowering of resonant frequency, as shown in Fig. 4b). The proposed H_1 is valid for the resonant frequency within the range defined by the critical frequency $F_s/6$ and Nyquist frequency $F_s/2$.

Owing to ten-time oversampling implementation, the ratio of computational frequency of the backward-Euler discrete derivative implementation to resonant frequency F_{res} is 40. With this large value, it can be known that the discrete-time difference equation implementation will preserve the discrete-time frequency characteristics near and below F_{res}, somewhat similar to what has been shown in Fig. 5. Note that the 25 kHz sampling frequency only applies to capacitor voltage measurement, the discrete derivative calculation, and the cascaded first-order low-pass filter calculations. It means for every tenth set of these calculations, the main current control controller and PWM will only be executed once. In the subsequent implementation, $H_1(s)$ with $m = 2$ is therefore chosen as the candidate for implementation. The chosen cascaded low-pass filter (implemented at $10F_s$ Hz) effectively provides a simple, second-order noise filtering to the experimental measurement noise.

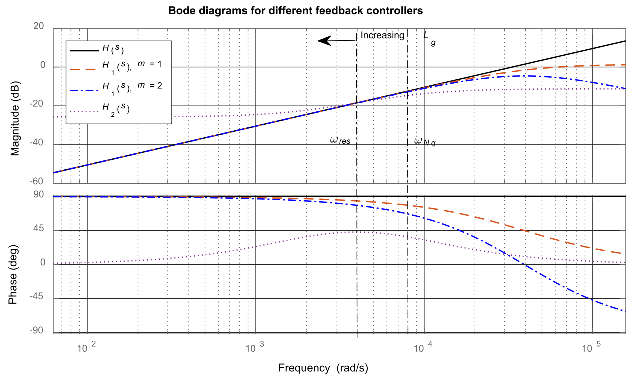

FIGURE 5. Bode diagrams for the (black, solid line) perfect differentiator H, (long-dashed line) oversampled-differentiator with single low-pass filters H_1, (long-short-dashed line) oversampled-differentiator with cascaded low-pass filters H_1, and (short-dashed line) lead compensator H_2 [7].

Tuning of the PI gains is due for consideration: symmetrical optimum tuning [6] is applied here. The approximation can be done by assuming an L inductor and ignoring the presence of C capacitor. The plant model can then be reduced to a first-order nature. With the sampling-based implementation at F_s approximated as a first-order delay, the plant can be modelled as:

$$T_{CL}(s) = \frac{1}{sL_T(T_1 s + 1)} \tag{16}$$

$L_T = (L_1 + L_2)$ and $T_1 = 1/F_s$. Then, the PI gains can be estimated using the symmetrical optimum tuning [7]:

$$K_p = \frac{L_T}{aT_1} \qquad \tau_i = a^2 T_1 \tag{17}$$

The standard recommended range of a is 2 to 4 [7], and a value of 4 is used to obtain the initial estimate of K_p and K_i values. Then, they are slightly fine-tuned in the experiments

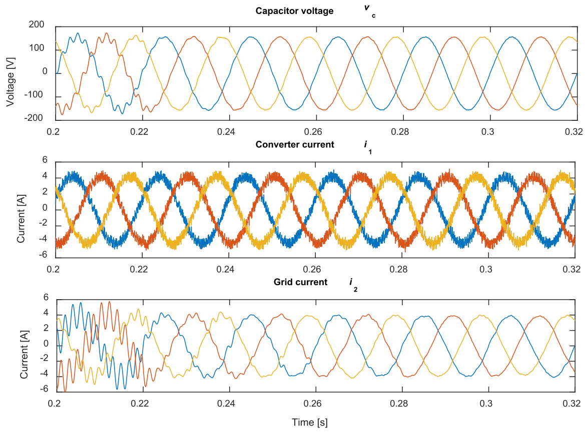

FIGURE 6. FCS-MPC – active damping performance for w_2 being 0, 10, 20, 50, 100, and 150 in every consecutive fundamental period (start from 0.2s). Grid current references are i_{2d}^* =$_{2q}^*$= 0 A.

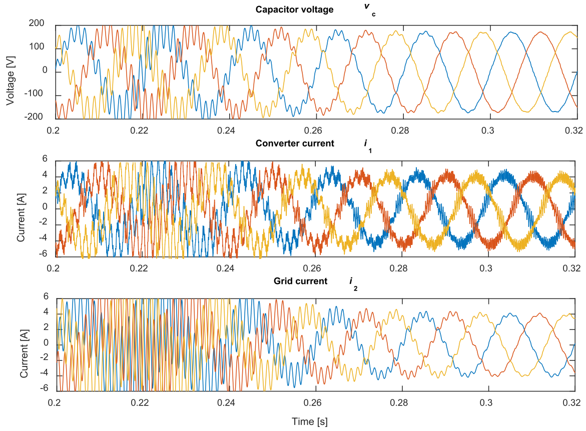

FIGURE 7. D-PI-PWM control – active damping is activated at 0.22s by setting K_{ad} as 5. Grid current references are $i_{2d}^* = 4$ A and $i_{2q}^* = 0$ A.

to account for the model error due to the presence of non-zero L_g. Lastly, the converter current reference is obtained in the same manner as the FCS-MPC counterpart, i.e. through reactive power compensation principle.

IV. SIMULATION RESULTS

A. SYSTEM PARAMETERS

The system parameters used in the simulation and experimental setup are listed in Table 1. With limited DC power supply, the experiments are conducted with a three-phase 208V-50Hz grid using a variac and an isolation Δ-Y transformer. All the measured current and voltage variables are normalized to the base values. This necessitates base values to be appropriately introduced in the state, control input, and disturbance input state-matrices in (1)-(2), and in the capacitor voltage and converter current references setting in (7)-(14).

B. STEADY-STATE, TRANSIENT, AND ACTIVE DAMPING PERFORMANCE

Fig. 6 shows the impacts of different weighting factor w_2 value on the active damping performance. Throughout the test, the d-axis grid current reference is set to 4 A, i.e. injecting active power to the grid. Before time 0.22 s, the active damping is off and it can be seen clearly that despite a regulated converter current (i.e. remains sinusoidal in shape), the grid current and the capacitor voltage contain a dominant resonance harmonic that corresponds to L_2C resonant frequency (confirmed by FFT). As the weighting factor w_2 changes to 10, the resonance is damped slightly but large distortions are still present. As w_2 changes from 10 to higher values, the resonance then reduces to a sufficiently low level. On other hand, a similar test is done for the D-PI-PWM control scheme (based on the controller design and gain setting recommended in Section III) with K_{ad} changed from 0 to 5 at 0.22 s. Fig. 7 demonstrates that the active damping functions as expected. It is obvious that the multivariable cost-function-based active damping of FCS-MPC has a much smaller time constant as compared to that of D-PI-PWM, and that their nature of undamped resonance is somewhat different (Figs. 6–7, before 0.22 s, being marginally stable in the former versus being unstable in the latter).

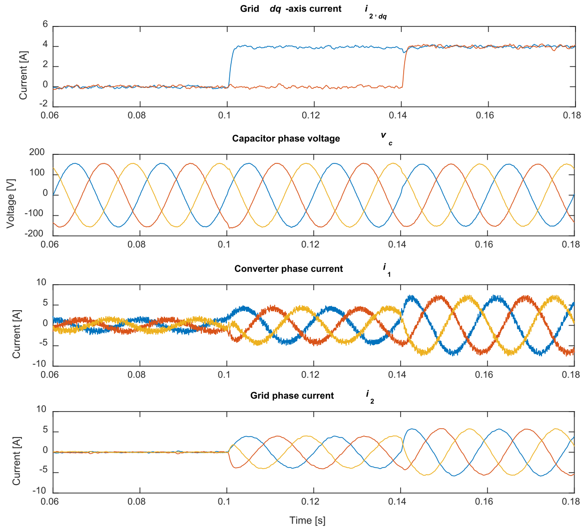

FIGURE 8. FCS-MPC – transient performance with the default setting (Table 1). i_{2d}^* is stepped from 0 to 4 A at time 0.1 s; then, i_{2q}^* is stepped from 0 to 4 A at time 0.14 s. w_2 is set as 100.

On the other hand, the transient performances of FCS-MPC (with $w_2 = 100$) and D-PI-PWM (with $a = 4$ and $K_{ad} = 5$) are shown in Figs. 8 and 9, respectively. Two step-changes are introduced for FCS-MPC scheme: d-axis grid current reference steps from 0 to 4 A at 0.1 s (0.2 s for D-PI-PWM); then, q-axis grid current reference steps from 0 to 4 A at 0.14 s (0.24 s for D-PI-PWM). The results clearly demonstrate the high-quality dynamic performance of FCS-MPC as, unlike those for D-PI-PWM scheme, no low-order oscillation is seen after each stepping.

C. CRITICAL FREQUENCY CONSIDERATION

Performance of the FCS-MPC scheme at the critical operating point is analyzed next. Critical frequency is defined as $1/(4T_d)$ where T_d is the total time delay. D-PI-PWM control has a digital implementation delay of $1.5T_s$ [1]–[22]

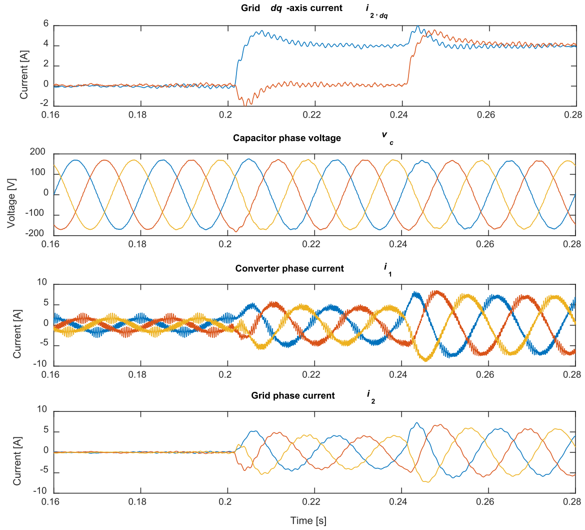

FIGURE 9. **D-PI-PWM control – transient performance. i_{2d}^* is stepped from 0 to 4 A at time 0.2 s; then, i_{2q}^* is stepped from 0 to 4 A at time 0.24 s. K_{ad} is set as 5.**

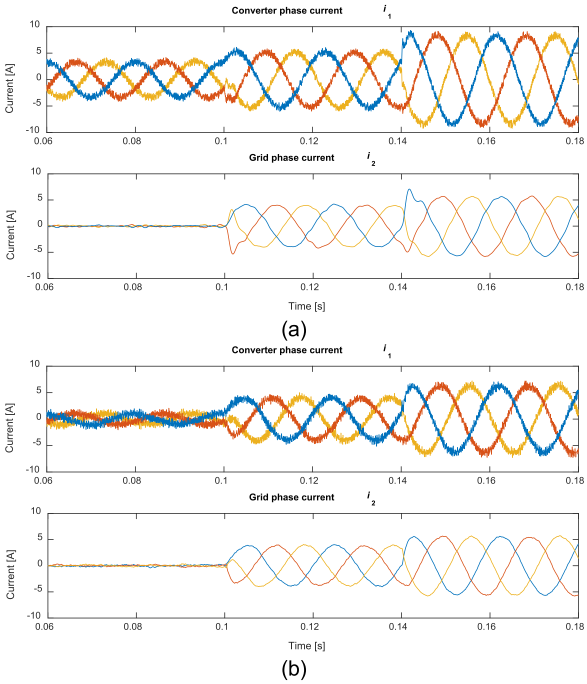

FIGURE 10. **FCS-MPC control – critical frequency consideration. (a) $C = 70\ \mu F$, i.e. $F_{res} = 415$ Hz ($<F_{crit\_MPC}$) and (b) $C = 20\ \mu F$, i.e. $F_{res} = 777$ Hz ($>F_{crit\_MPC}$). Same reference and w_2 settings as those in Fig. 8.**

hence its critical frequency F_{crit_PWM} is 417 Hz. On the other hand, FCS-MPC has a delay of T_s (without the $0.5T_s$ PWM delay) hence its critical frequency F_{crit_MPC} is estimated to be 625Hz (based on the established understanding from frequency-domain techniques without taking into account the effect of predictive-based delay compensation). The capacitance C used for the case in Section IV-B is 30 μF and the resonant frequency $F_{res} = 634$ Hz. This means that Figs. 6 and 8 essentially correspond to the operating point of $F_{res} \approx F_{crit\_MPC}$. In addition, Fig. 10 shows the results for two more cases of resonance frequencies: 415 Hz ($<F_{crit\_MPC}$) and 777 Hz ($>F_{crit\_MPC}$). These resonance frequencies are obtained by setting C as 70 μF and 20 μF. It is clearly shown that FCS-MPC, whose delay has been accurately compensated using the one-step-ahead estimation, can seemingly perform better throughout the resonant frequency ranges and across the critical frequency. This is a somewhat different behavior as compared to the standard frequency-domain techniques. The existing theoretical understanding on D-PI-PWM control reveals that the active damping performance would deteriorate at the critical frequency operating point and more-robust compensation techniques such as that in [11], [12], [14] would usually be needed (but this is beyond the scope of this work). With the above finding, the experimental investigation will proceed with the setting of $C = 30\ \mu$F - being common for both control schemes. This is an interesting operating point to consider as F_{res} ($= 634$ Hz) is located above F_{crit_PWM} ($= 417$ Hz) but is practically the same as F_{crit_MPC} ($= 625$ Hz).

V. EXPERIMENTAL RESULTS

Fig. 11 shows the laboratory test rig for the comparative study. In all the experimental results, line-to-line (between phase-*a* and phase-*b*) quantities for the capacitor and grid voltages, and phase-*a* quantities for the converter and grid currents, are measured.

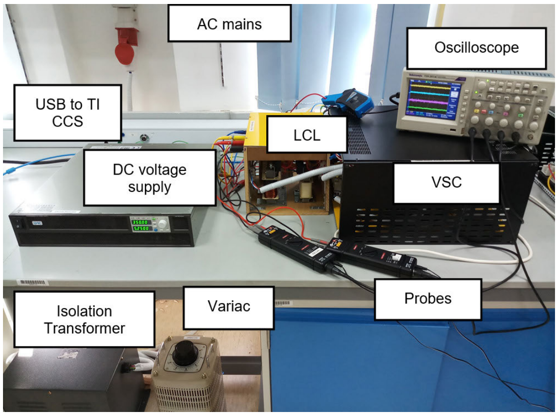

FIGURE 11. **Laboratory test rig for the grid-connected voltage source converter with an LCL filter. Both control strategies are tested using the same test rig under identical experimental setting.**

For the experimental FCS-MPC study, weighting factor w_2 is set as 0 to 50, in steps of 10. It was found that beyond 50, the controller becomes highly sensitive to the measurement accuracy since FCS-MPC is fundamentally trying to regulate the capacitor voltage in a weak-grid setting, which then leads to instability in synchronization. Hence, w_2 must be detuned in the experiment for final adoption. The schematic for the D-PI-PWM control strategy has been shown in Fig. 3, and the experimental settings are summarized in Table 1. The control sampling frequency is 2.5 kHz – being close to the average switching frequency of FCS-MPC scheme (to be detailed in Section V-E).

A. ACTIVE DAMPING PERFORMANCE

Capacitor voltage, converter current, grid voltage, and grid current for FCS-MPC with w_2 being 0 and 30 are shown in Fig. 12 (the case for $w_2 = 40$ will be shown in Fig. 15b). It clearly demonstrated that at $w_2 = 0$, significant resonance occurs between the capacitor voltage and grid current while the converter current exhibits sinusoidal shape, agreeing with the simulation findings. Since the grid interface is an isolation transformer, the grid is fundamentally a weak grid and the grid voltage is to some extent also distorted by the filter resonance. Upon the activation of cost-function-based active damping, the resonance can be suppressed.

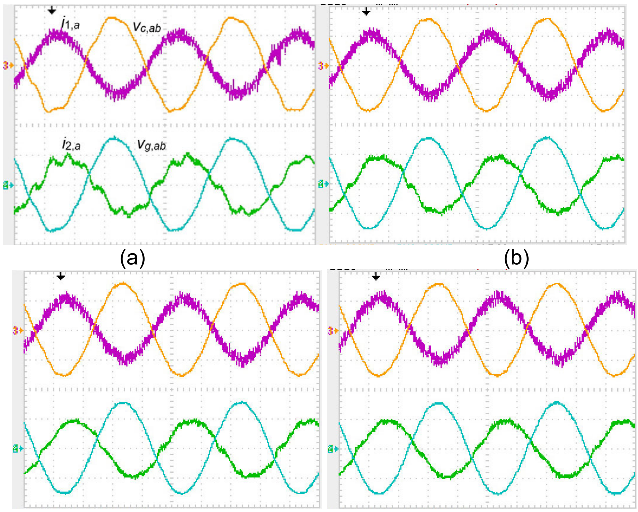

(a) (b)
(c) (d)

FIGURE 12. FCS-MPC experiment – w_2 is set to (a) 0, (b) 10, (b) 20, and (c) 30. Legend: (top pairs) capacitor line-to-line voltage $v_{c,ab}$ and converter phase-*a* current $i_{1,a}$; (bottom pairs) grid line-to-line voltage $v_{g,ab}$ and grid phase-*a* current $i_{2,a}$.

On the other hand, Fig. 13 shows the equivalent counterpart results for D-PI-PWM control strategy. K_{ad} of 10, being slightly different from the simulation value but is still within the range recommended by the theoretical study, is used here. It is shown that prior to the activation of the auxiliary active damping loop, not only that the capacitor voltage and grid current contain the high-order resonant harmonics (which are already higher than that of FCS-MPC), the converter current is also significantly distorted. This agrees with the simulation findings and is different from that the behavior shown by FCS-MPC. This can be explained by the low bandwidth nature of the main PI-based current controllers, being about 115 Hz (in theory, determined separately from the simulation's closed-loop bode diagram). Upon the activation of the active compensation, the resonance is suppressed successfully.

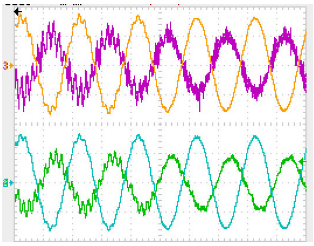

FIGURE 13. D-PI-PWM Control's active damping activation – K_{ad} is changed from 0 to 10. Legend as in Fig. 12.

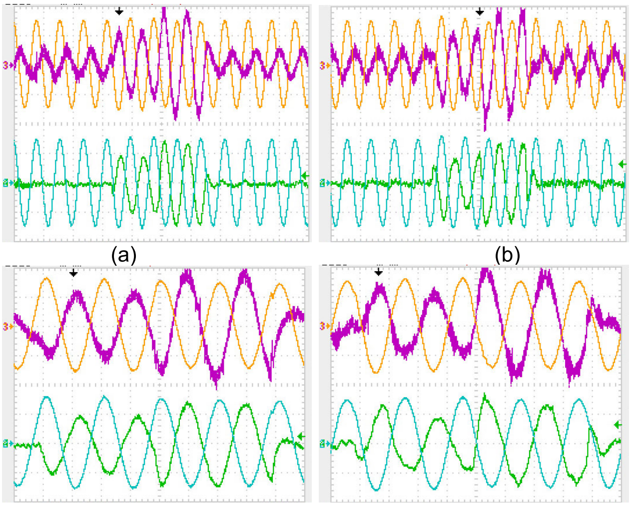
(a) (b)
(c) (d)

FIGURE 14. Transient experiment – (a) FCS-MPC with $w_2 = 40$; (b) D-PI-PWM control with $K_{ad} = 10$. i_{2d}^* is first stepped from 0 A to 4 A and then it is followed by i_{2q}^* being stepped to 0 A to 4 A after two fundamental cycles. Top plots are the long duration view and bottom plots are the zoom-in view of a separate recording. Legend as in Fig. 12.

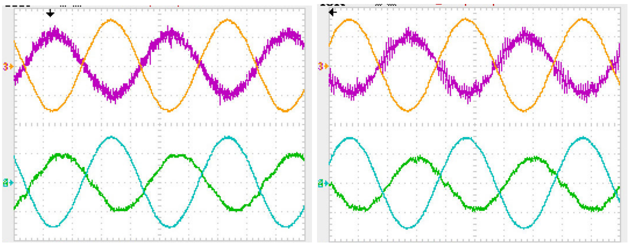
(a) (b)

FIGURE 15. Experimental steady-state waveforms for the operating point of $i_{2d}^* = 4$ A and$i_{2q}^* = 0$ A. (a) FCS-MPC with $w_2 = 40$; (b) D-PI-PWM control with $K_{ad} = 10$. Legend as in Fig. 12.

B. TRANSIENT PERFORMANCE

Next, the transient performance of FCS-MPC is shown in Fig. 14a and a zoomed-in extract is shown in Fig. 14c. The *d*-axis grid current reference is first stepped from 0 to 4 A, then followed by the *q*-axis grid current reference being stepped from 0 to 4 A after two fundamental cycles (i.e. 0.04 s). The same has been repeated for D-PI-PWM control and the result is shown in Figs. 14b and 14d. It can also be seen that when the current references are zero, the grid current is indirectly regulated to zero in both control strategies. This verifies the successful compensation of the reactive power needed by the *LCL* filter from the VSC. It is revealed that FCS-MPC produces excellent transient performance with

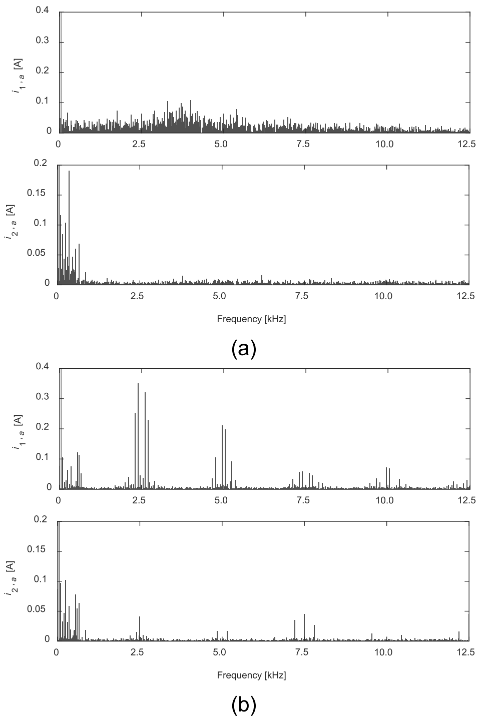

(a)

(b)

FIGURE 16. **Experimental FFT – frequency spectrum of phase-*a* (top) converter and (bottom) grid currents for (a) FCS-MPC and (b) D-PI-PWM control at the operating point with $i_{2d}* = 4$ A and $i_{2q}* = 0$ A.**

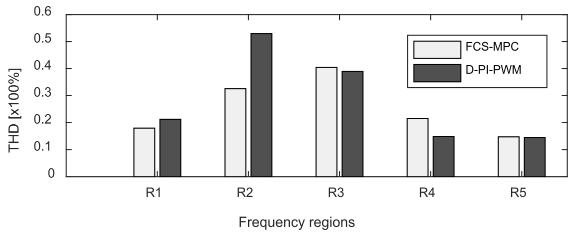

FIGURE 17. **Converter currents' harmonic distribution across the frequency spectrum. Region R1 is for 0.1 to 1.25 kHz region. From 1.25 kHz onwards, each of the R2 to R7 regions occupies the consecutive 2.5 kHz-wide frequency range, until 11.25 kHz.**

practically no overshoot while D-PI-PWM control produces approximately 40% overshoots. It should be highlighted that both control strategies adopted the same practical assumption of adopting zero grid impedance at the design stage. Yet, the high control bandwidth of FCS-MPC can mitigate any significant overshoot that could occur during transients.

C. STEADY-STATE PERFORMANCE

Steady-state performance is compared next. Fig. 15 shows the close views of the voltage and current waveforms for the two control strategies. For all practical purposes, they are comparable in practice. FFT of the phase-*a* converter and grid currents are obtained and displayed in Fig. 16a (FCS-MPC) and Fig. 16b (D-PI-PWM control). The useful region for comparison is only up to 10 kHz – being the Nyquist frequency of FCS-MPC. It is clearly seen that FCS-MPC produces the broad-spectrum switching harmonics while D-PI-PWM control produces the standard discrete-spectrum switching harmonics.

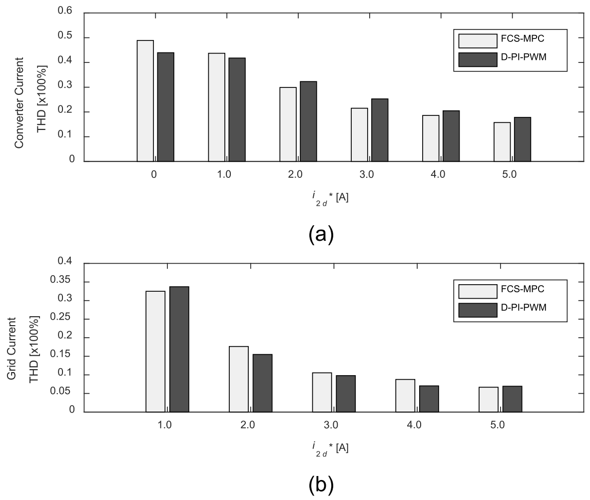

(a)

(b)

FIGURE 18. **THD comparison for different operating points at unity power factor (i.e. i_{2q}^* =0 A): (a) Converter phase-*a* current; (b) grid phase-*a* current.**

In order to gain further insight, the converter current switching harmonics are further categorized into total harmonic distortion (THD) values of different frequency regions and are re-plotted in Fig. 17. These THD values are obtained by root-squared-sum of all the harmonic components within the designated regions. Region R1's THD value is obtained by taking the square root of the squared sum of all the individual harmonic components between 100 Hz (i.e. after excluding the fundamental component) and 1.25 kHz. Region R2's THD value is obtained by taking the square-root of the squared sum of all the individual harmonic components within 1.25 kHz and 3.75 kHz; Subsequent regions' THD values take the same form for every 2.5 kHz range, until 11.25 kHz. This analysis clearly reveals that even though FCS-MPC has a broad switching harmonic spectrum in Region R2, its THD value is still lower than that of the main switching harmonics of D-PI-PWM.

The THD performance of the converter- and grid-current at different loading (i.e. for *d*-axis grid current's magnitudes of 0, 1, 2, 3, 4 and 5 A) is summarized in Fig. 18. The THD values are calculated in the same manner as that in Fig. 17. For all practical purposes, it is clearly shown that both control strategies have similar load-dependent THD values.

D. ACTIVE DAMPING PERFORMANCE OF FCS-MPC FOR DIFFERENT LCL PARAMETERS

FCS-MPC has a broad switching-harmonic spectrum, which makes the selection of LCL parameters and resonance frequency (F_{res}) somewhat more complex as compared to the fixed-switching-frequency control counterparts. What follows uses the average switching frequency ($F_{sw,average}$) of the FCS-MPC as the guideline to determine F_{res} value.

TABLE 2. Summary of the comparative assessment.

Feature	FCS-MPC	D-PI-PWM
Design domain	Discrete-time, state space	Frequency, transfer function
Parameter requirement during design	All, except grid impedance due to grid-voltage feedforward	All
# of gains to be tuned	One	Three
Main current tracking and dynamic tuning	Cost function based optimal control, no tuning required	PI-based feedback control, symmetrical optimum tuning
Active damping mechanism and tuning	Cost function, intuitive tuning	Multi-loop feedback control, using frequency-domain analysis
Practical consideration	No derivative control required	Discrete derivative's stability issue, require modified controller
Stability around F_{crit} (based on F_{crit} = 1/4T$_d$ definition)	Stable for delay-compensated predictive control	Critically stable, but Advanced techniques are required, e.g. [11, 12, 14]
Transient performance	Consistently very fast due to high control bandwidth	PI gains dependent, and will be affected more by L_g shifting
Switching frequency and harmonics	Varying, broad and continuous	Fixed, discrete and quantized

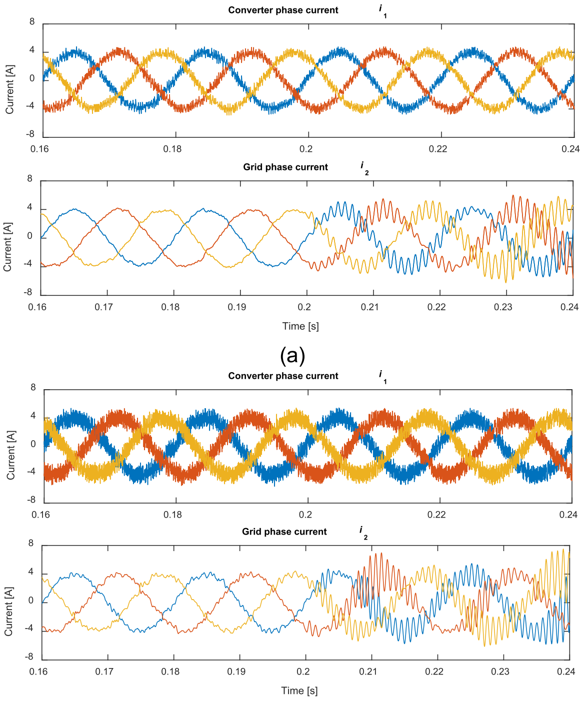

(a)

(b)

FIGURE 19. FCS-MPC's active damping performance for the following filter parameters (simulation): (a) $L_1 = 7.35$ mH, $C = 10\ \mu$F, and $L_2 = 2.94$ mH; (b) $L_1 = 2$ mH, $C = 10\ \mu$F, and $L_2 = 2$ mH. Current reference setting as in Figs. 6 and 7.

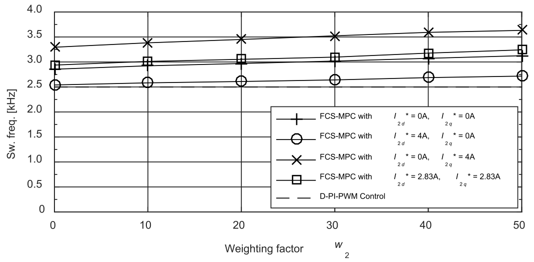

FIGURE 20. VSC's average switching frequency variation (over 1s period) as w_2 changes from 0 to 50.

In the preceding investigation, the designed F_{res} is slightly above ten times of the fundamental frequency. The $F_{sw,average}/F_{res}$ ratio is about four – within the typical ranges [33]. In order to further validate the robustness of the FCS-MPC's cost-function-based active damping feature (being a less understood subject as compared to the classical PWM-based counterparts), two other sets of LCL parameters are further considered here in the simulation studies:

(i) $L_1 = 7.35$ mH, $C = 10\ \mu$F, and $L_2 = 2.94$ mH ($F_{res} \approx 1.1$ kHz, $F_s = 20$ kHz, $F_{sw,average}/F_{res} \approx 3.4$); and
(ii) $L_1 = 2$ mH, $C = 10\ \mu$F, and $L_2 = 2$ mH ($F_{res} \approx 1.6$ kHz, $F_s = 40$ kHz, $F_{sw,average}/F_{res} \approx 4.7$).

F_s in case (ii) has been changed from 20 kHz to 40 kHz so that the $F_{sw,average}/F_{res}$ ratio is maintained well above two [33]. If one were to execute case (ii) with $F_s = 20$ kHz, the obtained $F_{sw,average}/F_{res}$ (through post-simulation analysis) is only about 2.3, which is somewhat too low in practice. The grid current switching harmonics will be too high for practical acceptance. Weighting factor w_2, which is not the focus in this subsection, is set empirically as 20. The steady-state active damping performance for the two cases are summarized in Fig. 19. It can be seen that prior to 0.2 s, the active damping functions as expected. Upon turning off the active damping feature (i.e. by setting $w_2 = 0$), the grid current resonates in both cases. This result essentially verifies that the effectiveness of the multivariable-cost-function-based active damping feature of FCS-MPC can be easily extended for a wider choice of filter parameters. Moreover, the converter current waveforms in Fig. 19 exhibit a low level of resonant components, which once again reflects the high control bandwidth nature of FCS-MPC in regulating the converter current – this agrees with the previous findings.

E. OTHERS

FCS-MPC's average switching frequency is analyzed next. Four different current references scenarios are implemented in the experiments, and the averaged switching frequency (per second) for different w_2 values are recorded, as summarized in Fig. 20. It is found that the d-axis and q-axis grid current references have opposite effects on the average switching frequency, but the general trend is that as weighting factor w_2 increases, the average switching frequency increases. Since the common operational settings correspond to the one with unity power factor, i.e. q-axis grid current being zero, the FCS-MPC's switching frequency of about 2.5 kHz is chosen as the control/switching frequency for D-PI-PWM in all previous studies. To conclude the comparative assessment, most of the considered features are summarized in Table 2.

VI. CONCLUSION

Finite-control-set model predictive control has recently made its way into grid-connected applications with active damping consideration. In this paper, FCS-MPC with cost-function-based active damping has been compared with the classical PI-based synchronous current control with derivative-voltage-based active damping. The active damping design analysis of FCS-MPC remains in the time-domain while D-PI-PWM control counter requires the frequency-domain analysis. Both control schemes required identical measurement requirements and have been tested in the same experimental test rig. It is evidenced that the FCS-MPC scheme is able to produce similar steady-state performance as the state-of-the-art counterpart. It is also found that the level of active damping can be intuitively tuned and fast current tracking is naturally guaranteed in FCS-MPC. In addition, the delay-compensated FCS-MPC is also found to be stable at its critical frequency (being $F_s/4$), somewhat in contrast to the standard feedback control that are known to deteriorate at the critical frequency (being $F_s/6$, and advanced robust compensation techniques [11], [12], [14] are relevant). Although the computational effort with respect to the available computational period under equal (almost) switching frequency condition is higher in FCS-MPC, but the continuous advancement of microprocessors has alleviated this concern. Lastly, this comparative study has essentially shown that the performance of FCS-MPC on simultaneous fundamental current and active damping control is comparable with that of the state of the arts. This therefore justifies the potential of FCS-MPC in this specific application and the needs for further improvements. Recommended future works for FCS-MPC improvement include modelling of measurement noise for analytical weighting factor tuning, improving the broad-spectrum switching harmonics to suit the existing fixed-switching-frequency LCL filter design guidelines [29], further investigating the robustness to parameter deviation, and investigating the unbalanced and high-order harmonic current tracking performance.

REFERENCES

[1] W. Wu, Y. Liu, Y. He, H. S.-H. Chung, M. Liserre, and F. Blaabjerg, "Damping methods for resonances caused by LCL-filter-based current-controlled grid-tied power inverters: An overview," *IEEE Trans. Ind. Electron.*, vol. 64, no. 9, pp. 7402–7413, Sep. 2017.

[2] R. Peña-Alzola, M. Liserre, F. Blaabjerg, R. Sebastián, J. Dannehl, and F. W. Fuchs, "Systematic design of the lead-lag network method for active damping in LCL-filter based three phase converters," *IEEE Trans. Ind. Informat.*, vol. 10, no. 1, pp. 43–52, Feb. 2014.

[3] R. Peña-Alzola, M. Liserre, F. Blaabjerg, M. Ordonez, and T. Kerekes, "A self-commissioning notch filter for active damping in a three-phase LCL-filter-based grid-tie converter," *IEEE Trans. Power Electron.*, vol. 29, no. 12, pp. 6754–6761, Dec. 2014.

[4] W. Yao, Y. Yang, X. Zhang, F. Blaabjerg, and P. C. Loh, "Design and analysis of robust active damping for LCL filters using digital notch filters," *IEEE Trans. Power Electron.*, vol. 32, no. 3, pp. 2360–2375, Mar. 2017.

[5] E. Rodriguez-Diaz, F. D. Freijedo, J. C. Vasquez, and J. M. Guerrero, "Analysis and comparison of notch filter and capacitor voltage feedforward active damping techniques for LCL grid-connected converters," *IEEE Trans. Power Electron.*, vol. 34, no. 4, pp. 3958–3972, Apr. 2019.

[6] J. Dannehl, M. Liserre, and F. W. Fuchs, "Filter-based active damping of voltage source converters with LCL filter," *IEEE Trans. Ind. Electron.*, vol. 58, no. 8, pp. 3623–3633, Aug. 2011.

[7] J. Dannehl, F. W. Fuchs, S. Hansen, and P. B. Thøgersen, "Investigation of active damping approaches for PI-based current control of grid-connected pulse width modulation converters with LCL filters," *IEEE Trans. Ind. Appl.*, vol. 46, no. 4, pp. 1509–1517, Jul./Aug. 2010.

[8] Z. Xin, P. C. Loh, X. Wang, F. Blaabjerg, and Y. Tang, "Highly accurate derivatives for LCL-filtered grid converter with capacitor voltage active damping," *IEEE Trans. Power Electron.*, vol. 31, no. 5, pp. 3612–3625, May 2016.

[9] D. Pan, X. Ruan, and X. Wang, "Direct realization of digital differentiators in discrete domain for active damping of LCL-type grid-connected inverter," *IEEE Trans. Power Electron.*, vol. 33, no. 10, pp. 8461–8473, Oct. 2018.

[10] C. Bao, X. Ruan, X. Wang, W. Li, D. Pan, and K. Weng, "Step-by-step controller design for LCL-type grid-connected inverter with capacitor–current-feedback active-damping," *IEEE Trans. Power Electron.*, vol. 29, no. 3, pp. 1239–1253, Mar. 2014.

[11] D. Pan, X. Ruan, C. Bao, W. Li, and X. Wang, "Capacitor-current-feedback active damping with reduced computation delay for improving robustness of LCL-type grid-connected inverter," *IEEE Trans. Power Electron.*, vol. 29, no. 7, pp. 3414–3427, Jul. 2014.

[12] D. Pan, X. Ruan, C. Bao, W. Li, and X. Wang, "Optimized controller design for LCL-type grid-connected inverter to achieve high robustness against grid-impedance variation," *IEEE Trans. Ind. Electron.*, vol. 62, no. 3, pp. 1537–1547, Mar. 2015.

[13] X. Li, X. Wu, Y. Geng, X. Yuan, C. Xia, and X. Zhang, "Wide damping region for LCL-type grid-connected inverter with an improved capacitor-current-feedback method," *IEEE Trans. Power Electron.*, vol. 30, no. 9, pp. 5247–5259, Sep. 2015.

[14] Y. He, X. Wang, X. Ruan, D. Pan, X. Xu, and F. Liu, "Capacitor-current proportional-integral positive feedback active damping for LCL-type grid-connected inverter to achieve high robustness against grid impedance variation," *IEEE Trans. Power Electron.*, to be published. doi: 10.1109/TPEL.2019.2906217.

[15] J. Liu, L. Zhou, and M. Molinas, "Damping region extension for digitally controlled LCL-type grid-connected inverter with capacitor-current feedback," *IET Power Electron.*, vol. 11, no. 12, pp. 1974–1982, Oct. 2018.

[16] L. Harnefors, A. G. Yepes, A. Vidal, and J. Doval-Gandoy, "Passivity-based controller design of grid-connected VSCs for prevention of electrical resonance instability," *IEEE Trans. Ind. Electron.*, vol. 62, no. 2, pp. 702–710, Feb. 2015.

[17] J. Yin, S. Duan, and B. Liu, "Stability analysis of grid-connected inverter with LCL filter adopting a digital single-loop controller with inherent damping characteristic," *IEEE Trans. Ind. Informat.*, vol. 9, no. 2, pp. 1104–1112, May 2013.

[18] J. Xu, S. Xie, and T. Tang, "Active damping-based control for grid-connected LCL-filtered inverter with injected grid current feedback only," *IEEE Trans. Ind. Electron.*, vol. 61, no. 9, pp. 4746–4758, Sep. 2014.

[19] X. Wang, F. Blaabjerg, and P. C. Loh, "Virtual RC damping of LCL-filtered voltage source converters with extended selective harmonic compensation," *IEEE Trans. Power Electron.*, vol. 30, no. 9, pp. 4726–4737, Sep. 2015.

[20] X. Wang, F. Blaabjerg, and P. C. Loh, "Grid-current-feedback active damping for LCL resonance in grid-connected voltage-source converters," *IEEE Trans. Power Electron.*, vol. 31, no. 1, pp. 213–223, Jan. 2016.

[21] T. Liu, J. Liu, Z. Liu, and Z. Liu, "A study of virtual resistor-based active damping alternatives for LCL resonance in grid-connected voltage source inverters," *IEEE Trans. Power Electron.*, to be published. doi: 10.1109/TPEL.2019.2911163.

[22] S. Leitner, M. Yazdanian, S. Ziaeinejad, A. Mehrizi-Sani, and A. Muetze, "Internal model-based active resonance damping current control of a grid-connected voltage-sourced converter with an LCL filter," *IEEE Trans. Power Syst.*, vol. 33, no. 6, pp. 6025–6036, Nov. 2018.

[23] N. Mukherjee and D. De, "Analysis and improvement of performance in LCL filter-based PWM rectifier/inverter application using hybrid damping approach," *IET Power Electron.*, vol. 6, no. 2, pp. 309–325, Feb. 2013.

[24] J. Ye, A. Shen, Z. Zhang, J. Xu, and F. Wu, "Systematic design of the hybrid damping method for three-phase inverters with high-order filters," *IEEE Trans. Power Electron.*, vol. 33, no. 6, pp. 4944–4956, Jun. 2018.

[25] J. Scoltock, T. Geyer, and U. K. Madawala, "A model predictive direct current control strategy with predictive references for MV grid-connected converters with LCL-filters," *IEEE Trans. Ind. Electron.*, vol. 30, no. 10, pp. 5926–5937, Oct. 2015.

[26] X. Zhang, Y. Wang, C. Yu, L. Guo, and R. Cao, "Hysteresis model predictive control for high-power grid-connected inverters with output LCL filter," *IEEE Trans. Ind. Electron.*, vol. 63, no. 1, pp. 246–256, Jan. 2016.

[27] P. Falkowski and A. Sikorski, "Finite control set model predictive control for grid-connected AC–DC converters with LCL filter," *IEEE Trans. Ind. Electron.*, vol. 65, no. 4, pp. 2844–2852, Apr. 2018.

[28] N. Panten, N. Hoffmann, and F. W. Fuchs, "Finite control set model predictive current control for grid-connected voltage-source converters with LCL filters: A study based on different state feedbacks," *IEEE Trans. Power Electron.*, vol. 31, no. 7, pp. 5189–5200, Jul. 2016.

[29] X. Zhang, L. Tan, J. Xian, H. Zhang, Z. Ma, and J. Kang, "Direct grid-side current model predictive control for grid-connected inverter with LCL filter," *IET Power Electron.*, vol. 11, no. 15, pp. 2450–2460, Dec. 2018.

[30] R. Guzman, L. G. de Vicuña, A. Camacho, J. Miret, and J. M. Rey, "Receding-horizon model-predictive control for a three-phase VSI with an LCL filter," *IEEE Trans. Ind. Electron.*, vol. 66, no. 9, pp. 6671–6680, Sep. 2019.

[31] M. G. Judewicz, S. A. González, J. R. Fischer, J. F. Martínez, and D. O. Carrica, "Inverter-side current control of grid-connected voltage source inverters with LCL filter based on generalized predictive control," *IEEE Trans. Emerg. Sel. Topics Power Electron.*, to be published. doi: 10.1109/JESTPE.2018.2826365.

[32] X. Yuan, W. Merk, H. Stemmler, and J. Allmeling, "Stationary-frame generalized integrators for current control of active power filters with zero steady-state error for current harmonics of concern under unbalanced and distorted operating conditions," *IEEE Trans. Ind. Appl.*, vol. 38, no. 2, pp. 523–532, Mar./Apr. 2002.

[33] M. Liserre, F. Blaabjerg, and S. Hansen, "Design and control of an LCL-filter-based three-phase active rectifier," *IEEE Trans. Ind. Appl.*, vol. 41, no. 5, pp. 1281–1291, Sep./Oct. 2005.

CHEE SHEN LIM (M'14) received the B.Eng. degree (Hons.) in electrical engineering from the University of Malaya, Malaysia, in 2009, and the joint-university Ph.D. degrees in power electronics and drives from the University of Malaya and Liverpool John Moores University, U.K., in 2013.

From 2009 to 2013, he was a Research Assistant with the Power Energy Dedicated Advanced Centre, University of Malaya. From 2013 to 2015, he was a Research Scientist with the Experimental Power Grid Centre, Agency for Science, Technology, and Research (A*STAR), Singapore. He is currently an Assistant Professor of electrical and electronic engineering with the University of Southampton Malaysia. His research interests include advanced model predictive control design, multiphase motor drives, grid-connected converter control, and microgrid hierarchical control. He also serves as an Associate Editor for the *IET Electric Power Applications*.

SZE SING LEE (SM'18) received the B.Eng. (Hons.) and Ph.D. degree in electrical engineering from Universiti Sains Malaysia, Malaysia, in 2010 and 2013, respectively.

From 2014 to 2019, he was a Lecturer/Assistant Professor with the University of Southampton Malaysia. From 2018 to 2019, he was a Visiting Research Professor with Ajou University, South Korea. He is currently an Assistant Professor of electrical and electronic engineering with Newcastle University, Singapore. His research interest includes power converter/inverter topologies and their control strategies.

Dr. Lee received the International Scholar Exchange Fellowship from the Korea Foundation for Advanced Studies, in 2018. He also serves as an Associate Editor for IEEE Access.

YI CHYN CASSANDRA WONG (S'18) received the B.Eng. degree (Hons.) in electrical power engineering from Curtin University, Malaysia, in 2016. She is currently pursuing the split-site Ph.D. degree with the University of Southampton, U.K., and the University of Southampton Malaysia.

She was a Research Intern with the Experimental Power Grid Centre, Agency for Science, Technology, and Research (A*STAR), Singapore, from August to October 2017. Her research interests include power quality improvement, optimization control, and distributed cooperative control in microgrid.

INAM ULLAH NUTKANI (SM'14) received the B.E. degree in electrical engineering from the NED University of Engineering and Technology, Karachi, Pakistan, in 2003, and the M.S. and Ph.D. degrees in electrical power engineering from Nanyang Technological University, Singapore, in 2007 and 2014, respectively. He has more than 12 years of professional work experience in different domains of power system with power utilities—K-Electric Karachi, industry—West Energy Singapore, consultancy firms—JM Pang and Seah Singapore, and research organizations—NESCOM Islamabad and Experimental Power Grid Centre, A*STAR Singapore, from 2003 to 2016. He is currently a Lecturer of electrical power systems and power electronics with the School of Engineering, Royal Melbourne Institute of Technology (RMIT), Melbourne, Australia. His research interests include renewable, distributed generation and microgrid, power electronics and control, and next-generation electricity grids.

HUI HWANG GOH (SM'12) received the B.Eng. (Hons.) and M.Eng. degrees in electrical engineering and the Ph.D. degree from the Universiti Teknologi Malaysia (UTM), Malaysia, in 1998, 2002, and 2007, respectively.

He is currently a Professor of electrical engineering with the School of Electrical Engineering, Guangxi University, Nanning, China. His research interests include embedded power generation modeling and simulation, power quality studies, wavelet analysis, multi-criteria decision making, renewable energies, and dynamic equivalent. He is also a Fellow of the Institution of Engineering and Technology (IET), U.K., the ASEAN Academy of Engineering and Technology (AAET), and the Institution of Engineers, Malaysia (IEM), a Chartered Engineer under the Engineering Council United Kingdom (ECUK), and a Professional Engineer under the Board of Engineers, Malaysia (BEM).

• • •